Annals of Nuclear Energy 211 (2025) 110956

Contents lists available at ScienceDirect

Annals of Nuclear Energy

journal homepage: www.elsevier.com/locate/anucene

Analysis of swarm flow and bubble residence time under pool scrubbing conditions

Fanli Kong *, Xu Cheng

Institute for Applied Thermofluidics (IATF), Karlsruhe Institute of Technology (KIT), Kaiserstrasse 12, 76131 Karlsruhe, Germany

ARTICLE INFO

Keywords:
Pool scrubbing
Swarm flow
Euler-Euler approach
Lagrangian approach
Bubble residence time

ABSTRACT

In severe accidents of nuclear power plants, large amounts of fission products existing as radioactive aerosols are released. Pool scrubbing plays an important role in the removal of radioactive aerosols. Bubble residence time is one of the key parameters to determine the efficiency of aerosol removal, especially in the swarm flow region which makes a very important contribution to the total aerosol removal. In this study, the Euler-Euler-Lagrangian approach is built to track the evolution of bubble motion and to determine the bubble residence time in the liquid pool. Specifically, the Euler-Euler two-fluid approach is utilized to resolve the flow field of gas and liquid phases, while the Lagrangian approach is employed to track the discrete bubbles and to obtain the bubble residence time. The results reveal that the present approach is feasible to predict the bubble dynamics and residence time in the liquid pool. Bubble residence time is dependent on the initial position, where bubbles deviating from the central region could remain inside the liquid pool for a longer physical time. The bubble diameter, volume flow rate and submergence height are key parameters affecting the bubble residence time. And comparison between the simulated bubble residence time and the model-predicted results is carried out, indicating the discrepancy of simulated residence time and limitations of the existing model at high volume flow rate and high submergence.

1. Introduction

In severe accidents of nuclear power plants, large amounts of gas-containing fission products existing as radioactive aerosols are released. Pool scrubbing process is one of the most effective measures to remove aerosols. It has gained more attention to the evaluation of the removal performance and the hydrodynamic phenomena of multiphase flow under pool scrubbing conditions (Gao et al., 2017; Yan et al., 2020). Based on the experimental observation, the process of pool scrubbing is divided into three regions: injection, transition and swarm flow (Abe et al., 2018), shown in Fig. 1. Gas with aerosols leaving a vent becomes large bubbles (globules) or continuous jet flow on the injection region and break up into a swarm of small bubbles (transition). Finally, the swarm bubbles rise to the pool surface. The aerosol is shifted from the gas phase to the liquid phase in the presence of the complex interaction between continuous water and discrete bubbles. As indicated in the reference (Owczarski and Burk, 1991), swarm flow contributes to a significant amount of aerosol decontamination due to a large gas–liquid contact area and long bubble residence time (Liao et al., 2022). And bubble residence time is highly important to determine aerosol decontamination efficiency. The decontamination performance is highly associated with hydrodynamic parameters such as geometric configuration, bubble rising velocity, and bubble residence time.

Due to its importance, some experiments were performed to investigate the detailed bubble hydrodynamic behavior. Abe et al. (2018) observed the flow structure and the aerosol particle behavior with different air flow rates. The detailed information on void fraction and gas velocity obtained by wire-mesh sensor provides a good reference for numerical research. Yoshida et al. (2022) investigated the interfacial area, three-dimensional velocity, and bubble diameter distribution in the same facility for further fundamental understanding. They recorded the bubble diameter distribution at different heights with various air flow rates and found that the number of bubbles increased with the bubble rising due to break-up and also with the increase of the air flow rate.

Apart from experimental works, some numerical works applied the CFD method to resolve the flow characteristics of the liquid pool. In terms of large-scale flow, the Euler-Euler two fluid method is widely applied to deal with complex two-phase flow. Bicer et al. (2021) checked void fraction distribution and air velocity for air inlet velocity of 150 m/s, they reported a receptible agreement in void fraction distribution

* Corresponding author.
E-mail address: fanli.kong@kit.edu (F. Kong).

https://doi.org/10.1016/j.anucene.2024.110956
Received 26 April 2024; Received in revised form 17 September 2024; Accepted 27 September 2024
Available online 7 October 2024

Nomenclature

A	area (m^2)
C	coefficient (−)
d	bubble diameter (m)
Eo	Eötvös number (−)
$\mathbf{F}$	interfacial force ($kg/(m^2 \cdot s)$)
$\mathbf{g}$	gravitational acceleration (m/s^2)
h	height (m)
m	mass (kg)
$\dot{m}$	mass flow rate (kg/s)
MRT	mean residence time (s)
N	equivalent bubble number (−)
p	pressure (Pa)
Q	total gas volume flow rate (L/s)
Re	Reynolds number (−)
RT	residence time (s)
Sr	dimensionless shear rate (−)
$\mathbf{U}$	velocity (m/s)
u	velocity component in x direction (m/s)
V	rising velocity (m/s)
v	velocity component in y direction (m/s)
w	velocity component in z direction (m/s)
We	Weber number (−)

Greek symbols

α	phase fraction (−)
γ	shear rate (s^{-1})
μ	dynamic viscosity ($kg/(m \cdot s)$)
ρ	density (kg/m^3)
σ	surface tension (N/m)
τ	stress tensor (m^2/s^2)
τ_r	particle relaxation time (s)

Superscript

*	normalization / nondimensionalization

Subscripts

a	air phase
b	bubble
c	cell
cap	cap shape
D	drag force
ellipse	ellipsoidal shape
H	major axis of ellipsoidal bubble
in	injection
i	index
k	phase
L	lift force
m	model
PG	pressure gradient force
r	relative
sphere	spherical shape
SW	swarm flow
T	terminal
TD	turbulent dispersion force
VM	virtual mass force
w	water phase
WL	wall lubrication

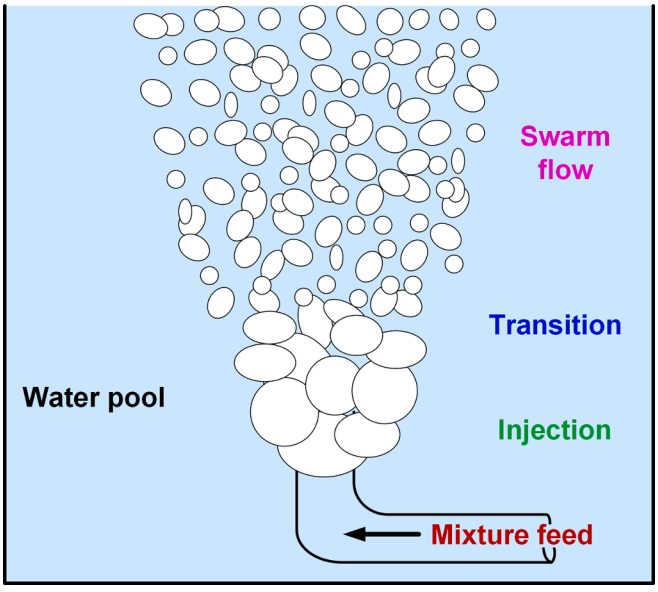

Fig. 1. Schematic diagram of hydrodynamic behavior during pool scrubbing.

between the experimental data and simulation results while the prediction of air velocity showed a large difference, especially for the injection region. The reasons are attributed to the turbulence modeling particularly the interfacial momentum models and the application of the constant bubble diameter model to represent poly-dispersed bubbles couldn't fully reflect the bubble interaction mechanism. The baseline models (Hänsch et al., 2021) with the utilization of Euler-Euler method offer the latest validated models by over 50 cases of pipe flows and bubble columns, consisting of interfacial force closure models including drag force, lift force, virtual mass force, turbulent dispersion force, wall lubrication force, turbulence model and poly-dispersity model like population balance model (PBM), bubble coalescence and breakup model, etc. Li et al. (2023) which applied the baseline model concluded that the bubble diameter is very important to simulate the pool scrubbing hydrodynamic when assuming it a monodispersed flow. Liao and Li (2023) and Bicer et al. (2023) also investigated the feasibility of the morphology-adaptive hybrid approach which combines the VOF (Volume Of Fluid) method and Euler-Euler two fluid method and evaluate the Interfacial Area Transport Equation (IATE) applicability in the high inlet velocity conditions, respectively.

Nevertheless, the Eulerian methodology cannot catch the phase interphase and individual bubble motion to get the bubble residence time. Interface capture methods include the VOF method and the Lagrangian particle tracking (LPT) method are usually used to simulate multiphase flow with individual bubbles and discrete flow (Chai and Cheng, 2015; Mei et al., 2022). Liao et al. (2022) applied the VOF method to model the gas jet flow of pool scrubbing. Limited discrepancies between the experimental data and simulation results have been found. However, the required computational cost is ever so large. In the experiment, it is also difficult to catch the motion of all the bubbles and record the bubble residence time with a high-speed camera because of bubble overlap and complex hydrodynamics phenomena including breakup and coalescence in the swarm region. The CFD simulation applied the LPT method could catch the individual bubble movement based on the Newton motion equations. The residence time distribution is then obtained from the movement tracks. The matched residence time results were acquired by employing the Euler-Euler-Lagrangian method (Le Moullec et al., 2008).

In this work, the simulation of swarm flow behavior and bubble

residence time under pool scrubbing conditions has been performed. The Euler-Euler-Lagrangian approach is built up in this work to track the evolution of bubble residence time in the liquid pool under pool scrubbing conditions. The Euler-Euler approach with the baseline model is used for the simulation of two-phase flow field. The Lagrangian approach based on the obtained flow field is employed to track the behavior of discrete bubbles and to obtain the bubble residence time. The effects of air inlet velocity, bubble diameter, volume flow rate, and submergence on bubble residence time are investigated.

2. Numerical approach and simulation settings

In the simulation of the entire swarm flow, the main aspects are the velocity and the residence time of the gas phase. Euler-Euler approach with Baseline models is used to predict the flow field evolution of pool scrubbing. Then the Lagrangian approach is applied in the obtained flow field to trace the bubble trajectory using the motion equation, which treats the bubble as the discrete phase, and to obtain the individual bubble residence time.

2.1. Euler-Euler approach

The Eulerian model solves the governing equations for each phase, both phases are considered as interpenetrating continua. The volume fraction of the gas phase is indeed resolved, but not the structure of the phase interface. In this work, it is assumed as incompressible and isothermal flow in the pool scrubbing process. The governing equations of mass and momentum can be written as follows:

$$\frac{\partial \alpha_k \rho_k}{\partial t} + \nabla \cdot (\alpha_k \rho_k \boldsymbol{U}_k) = 0 \tag{1}$$

$$\frac{\partial (\alpha_k \rho_k \boldsymbol{U}_k)}{\partial t} + \nabla \cdot (\alpha_k \rho_k \boldsymbol{U}_k \boldsymbol{U}_k) = \nabla \cdot (\alpha_k \tau_k) - \alpha_k \nabla p + \alpha_k \rho_k \mathbf{g} + \mathbf{F}_k \tag{2}$$

where subscript k represents the phase k; α, ρ, **U** are phase fraction, density and velocity respectively; τ, p, **g** are the stress tensor, pressure, and gravitational acceleration vector, respectively; $\mathbf{F}_k$ is the interface momentum transfer, the terms included in this work are shown as the right side of the bellowing equation, the drag force, lift force, virtual mass force, turbulent dispersion force, and wall lubrication force in order:

$$\boldsymbol{F}_k = \boldsymbol{F}_{\mathrm{D},k} + \boldsymbol{F}_{\mathrm{L},k} + \boldsymbol{F}_{\mathrm{VM},k} + \boldsymbol{F}_{\mathrm{TD},k} + \boldsymbol{F}_{\mathrm{WL},k} \tag{3}$$

All the selections of the interfacial force models and turbulence in the baseline model (Hänsch et al., 2021), are shown in Table 1.

2.2. Lagrangian approach

For the Lagrangian approach, the bubbles as dispersed phase are solved in a Lagrangian reference system. The force balance based on Newton's second law can be written as:

$$m_\mathrm{b} \frac{\mathrm{d}\boldsymbol{U}_\mathrm{b}}{\mathrm{d}t} = m_\mathrm{b} \frac{\boldsymbol{U}_\mathrm{w} - \boldsymbol{U}_\mathrm{b}}{\tau_\mathrm{r}} + m_\mathrm{b} \frac{\boldsymbol{g}(\rho_\mathrm{a} - \rho_\mathrm{w})}{\rho_\mathrm{a}} + \mathbf{F}_\mathrm{b} \tag{4}$$

Table 1
Model selection in current baseline models.

Item		Selection
Interfacial forces	Drag	Ishii and Zuber (1979)
	Lift	Hessenkemper et al. (2021)
	Virtual mass	Crowe et al. (2011)
	Turbulent dispersion	Burns et al. (2004)
	Wall lubrication	Hosokawa et al. (2002)
Turbulence	Bubble-induced	Ma et al. (2017)
	Shear-induced	k-omega-SST Menter et al. (2003)

where the subscript b and w denote bubble (the discrete phase) and water phase (the carrier phase) in our case, m_b is the mass of bubble, the terms on the right side are the drag force, the vertical combined force of gravity and buoyancy, and other additional forces such as lift force, virtual mass force, and pressure gradient force, etc. τ_r in drag force term is particle relaxation time. In this simulation, the drag force, gravity force, buoyancy force, lift force, virtual mass force, and pressure gradient force are considered. The drag force and lift force model selected in the Euler-Euler approach doesn't exist in the Lagrangian libraries. To keep consistent with the Euler-Euler approach, the drag force (Ishii and Zuber, 1979) and lift force model (Hessenkemper et al., 2021) were implemented in OpenFOAM in this work. τ_r in Eq. (5) is calculated by:

$$\tau_\mathrm{r} = \frac{\rho_\mathrm{a} d^2}{18 \mu_\mathrm{w}} \frac{24}{C_\mathrm{D} Re} \tag{5}$$

where d is the bubble diameter, μ_w is the dynamic viscosity of water phase, C_D is the drag force coefficient in selected model which is calculated by:

$$C_\mathrm{D} = \begin{cases} \min(C_{\mathrm{D,ellipse}}, C_{\mathrm{D,cap}}) & , C_{\mathrm{D,ellipse}} \geqslant C_{\mathrm{D,sphere}} \\ C_{\mathrm{D,sphere}} & , C_{\mathrm{D,ellipse}} < C_{\mathrm{D,sphere}} \end{cases} \tag{6}$$

with

$$\begin{aligned} C_{\mathrm{D,sphere}} &= \frac{24}{Re}\left(1 + 0.1 Re^{0.75}\right) \\ C_{\mathrm{D,cap}} &= \frac{2}{3}\sqrt{Eo} \\ C_{\mathrm{D,ellipse}} &= \frac{8}{3} \end{aligned} \tag{7}$$

where Reynolds number (Re) and Eötvös number (Eo) could be calculated by:

$$\begin{aligned} Re &= \frac{\rho_\mathrm{w} |\mathbf{U}_\mathrm{w} - \mathbf{U}_\mathrm{b}| d}{\mu_\mathrm{w}} \\ Eo &= \frac{\Delta \rho g d^2}{\sigma} \end{aligned} \tag{8}$$

where σ is the surface tension. The lift force is expressed as:

$$\mathbf{F}_{\mathrm{L,b}} = m_\mathrm{b} C_\mathrm{L} \frac{\rho_\mathrm{w}}{\rho_\mathrm{a}} (\mathbf{U}_\mathrm{w} - \mathbf{U}_\mathrm{b}) \times (\nabla \times \mathbf{U}_\mathrm{b}) \tag{9}$$

where C_L represents the lift force coefficient which is calculated as:

$$C_\mathrm{L} = f(Sr, Re) - f(Eo_\perp) \tag{10}$$

with

$$f(Sr, Re) = \left(\left(\frac{6}{\pi^2} \frac{1}{\sqrt{ReSr}} \frac{2.255}{(1 + 0.2\varepsilon^{-2})^{3/2}} \right)^2 + \left(0.5 \frac{Re + 16}{Re + 29} \right)^2 \right)^{1/2} \tag{11}$$

$$Sr = \frac{d\gamma}{|\mathbf{U}_\mathrm{c} - \mathbf{U}_\mathrm{b}|}, \varepsilon = \left(\frac{Sr}{Re} \right)^{1/2} \tag{12}$$

and

$$f(Eo_\perp) = \frac{\ln(1 + \exp(-12(G)))}{12} \tag{13}$$

$$G = 0.11 \frac{\ln(1 + \exp(4(Eo_\perp - 5.6)))}{4} - 0.14(Eo_\perp - 5.2) - 0.44 \tag{14}$$

$$Eo_\perp = \frac{\Delta \rho g d_\mathrm{H}^2}{\sigma} \tag{15}$$

$$d_H = d\sqrt[3]{1 + 0.63Eo^{0.35}} \tag{16}$$

Additional forces also include virtual mass force and pressure gradient force are expressed as following, respectively:

$$\mathbf{F}_{VM,b} = m_b C_{VM} \frac{\rho_w}{\rho_a} \left(\mathbf{U}_b \cdot \nabla \mathbf{U}_w - \frac{d\mathbf{U}_b}{dt} \right) \tag{17}$$

$$\mathbf{F}_{PG,b} = m_b \frac{\rho_w}{\rho_a} \mathbf{U}_b \cdot \nabla \mathbf{U}_w \tag{18}$$

where the virtual mass force coefficient (C_{vm}) is set as 0.5.

2.3. Simulation settings

Among the existing pool scrubbing experiments related to hydrodynamics, there are only several experiments (Abe et al., 2018; Yoshida et al., 2022) that have a relatively large scale and report detailed hydrodynamic data at the same time. Abe et al. (2018) measured the void fraction and velocity distribution at five different water heights in four cases with different gas injection velocities and volume flow rates which is helpful to validate and evaluate the numerical approach while this information was not provided by Yoshida et al. (2022). Therefore, in this work, the geometry and operating conditions are referred to the experiment of Abe et al. (2018). The test section is sized as 500 mm × 500 mm × 3000 mm which has a rectangular cross-section and the initial submergence (the distance from the nozzle to the water surface) is 1100 mm. The nozzle diameter is 6 mm. The experiment is operated at ambient conditions with different air volume flow rates, varying from 8.48, 42.4, 84.8, and 254.0 L/min (the corresponding air inlet velocities from the nozzle are 5, 25, 50, and 150 m/s, respectively). The time-averaged void fraction and air velocity distributions from 10 s sampling time at five height positions are obtained except in the second flow rate case.

As shown in Fig. 2, the whole computational domain in our work is W×L×H=500 mm × 500 mm × H. The submergence height H varies from 1.1 m to 3.1 m, to study its effect on the numerical results. The air section height of 0.4 m above the water surface is added to prevent the water flows out of the computational domain. The nozzle is a rectangular section, whose area is the same as a circle with a diameter of 6 mm. The investigated pool scrubbing process in this work is carried out at room temperature and ambient pressure. The air-water two-phase flow is assumed as the monodispersed flow and the constant bubble diameter is set in simulation. The maximum Courant number is set as 0.5 to adjust the time step. The total physical time is set as 30 s and the time range, which is used for calculating average results, is from 10 s to 30 s.

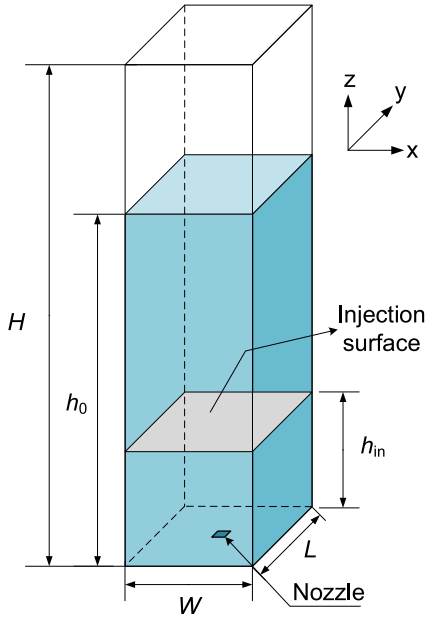

Fig. 2. Schematic diagram of computational domain.

After obtaining the time-averaged flow field, the Lagrangian approach was applied to get the bubble tracking and swarm bubble residence time. One-way coupling is utilized in this work, that is, the flow affects the bubble motion, but the effect of air bubbles on the water flow field was not involved in the Lagrangian part since the air–liquid flow has been simulated by Euler-Euler approach. Instead of that, the water flow field is mapped from the Euler-Euler approach to the Lagrangian approach. To investigate bubble residence time in the swarm region, the discrete bubble will be injected from each cell center of the surface where the swarm region begins (the gray plane shown in Fig. 2). For example, the swarm region in Abe's case is above the height of 300 mm according to the experimental observation (Abe et al., 2018), the injection surface with z = 300 mm as the injection height h_{in} is selected. Each bubble represents a group of bubbles injected in the same cell. To normalize the discrete bubble rising height, the bubble injected surface height is regarded as the initial level and is recorded as 0. Therefore, the normalized height is defined as:

$$h^* = \frac{h - h_{in}}{h_0 - h_{in}} \tag{19}$$

where h_{in} is the bubble injection height in Lagrangian bubble tracking part; h is the local height of bubble; h_0 is the submergence height, as shown in Fig. 2. The discrete phase is air bubble, and the information on the properties and velocity the individual bubble on the injection surface is gained from the Euler-Euler approach. Owing to the initial injection setup which uses one bubble to represent a group of bubbles from the same position, the actual mass flow rate is ignored here. The air mass flow rate in each cell could be calculated as:

$$\dot{m}_i = w_a \alpha_a \rho_a A_c \tag{20}$$

where w_a is the air vertical velocity and A_c is the cell area. After that, the equivalent bubble number of each cell could be converted from the mass flow rate and rounded as:

$$N_i = round\left(\frac{6\dot{m}_i}{\pi d^3 \rho_a} \right) \tag{21}$$

The specific numerical settings of Lagrangian approach are listed in Table 2. When evaluating the average residence time (*RT*), the mass flow rate should be taken back into consideration to reflect the real bubble number from each position. The mean residence time weighted by bubble number (*MRT*) is defined as:

$$MRT = \frac{\sum_{i=1}^{n} (RT_i \cdot N_i)}{\sum_{i=1}^{n} N_i} \tag{22}$$

where i is cell index.

Table 2
Numerical settings of Lagrangian approach.

Content	Variable	Value
Discrete phase: air bubbles	Diameter	3/4/5/6/8 mm
	Properties	Same as air phase in Euler-Euler part
Continuous phase: water	Properties	Same as water phase in Euler-Euler part
	Flow field	Same as water phase in Euler-Euler part
Injection models	Injection height	h^*=0 (z = 300 mm)
	Injection velocity	$u_b = u_a$, $v_b = v_a$, $w_b = w_a$
	Injection mass flow rate	Calculated by Eq. (20)

To evaluate the CFD results, the existing model in the numerical simulation code SPARC-90 (Owczarski and Burk, 1991), for calculating swarm rising velocity (m/s) and bubble residence time is introduced for comparison, i.e. swarm flow velocity:

$$V_{SW} = [(Q + 5.33)/3.011 \times 10^{-03}]^{1/2}(1 - 3.975 \times 10^{-02}h) \quad (23)$$

where Q is total gas volume flow rate (L/s) at half of h. The bubble residence time is then obtained by integrating the derivative of the velocity over the rise height as follows:

$$RT_m = \int_{h_{in}}^{h} \frac{1}{V_{SW}} dh \quad (24)$$

In order to dimensionless the residence time, the terminal velocity (V_T) of a single bubble in a stagnant fluid and total rising height are introduced as the characteristic velocity and length. Due to inertia dominant in this research, the expression of V_T is referred to Davies & Taylor equation (Daivies and Taylor, 1950) as Eq. (25), and the coefficient (C) is ignored.

$$V_T = C\sqrt{\frac{\Delta\rho g d}{\rho_w}} \quad (25)$$

Therefore, the dimensionless residence time (RT^*) is defined as:

$$RT^* = \frac{RT}{h_0 - h_{in}}\sqrt{\frac{\Delta\rho g d}{\rho_w}} \quad (26)$$

3. Evaluation of numerical approach

3.1. Validation of Euler-Euler approach

3.1.1. Mesh sensitivity study

To verify the simulation, the mesh independence is investigated for the air flow rate of 8.48 L/min (air inlet velocity is 5 m/s). The initial submergence height is 1.1 m and constant bubble diameter is set as 4 mm. The mesh in cross-section is refined around the nozzle because the flow structure is more concentrated in the central area according to the experimental observation while it is uniform in the vertical direction, as shown in Table 3. Fig. 3 shows the time-averaged void fraction in rising height z = 500 mm for different mesh numbers. There is little difference in the maximum void fraction value when radial node number comes to 70 but a small variation still exists in the range of void fraction distribution. The results are independent of the mesh resolution when the mesh number is over 1,280,000. Thus, the mesh with 1,280,000 cells is chosen for further research.

3.1.2. Comparison of Euler-Euler results with experiment data

The experiment data in air volume flow rates equal to 8.48 and 84.8 L/min of Abe et al. (2018) are selected for validation and comparison. The comparisons of time-averaged void fraction and air velocity for different air inlet velocities are shown in Fig. 4 ((a) 5 m/s; (b) 50 m/s). In Fig. 4 (a), the simulation has a good prediction in the trend of void fraction and velocity distribution, showing an unimodal trend of higher middle and decreasing outward. However, there is still a discrepancy in the maximum value and distribution range. the void fraction distributes in larger range and has a small peak value than experiment data above

Table 3
Mesh sensitivity study.

Mesh	Total mesh number	Radial node number	Axial node number
1	375,000	50	150
2	735,000	70	150
3	1,280,000	80	200
4	1,920,000	80	300

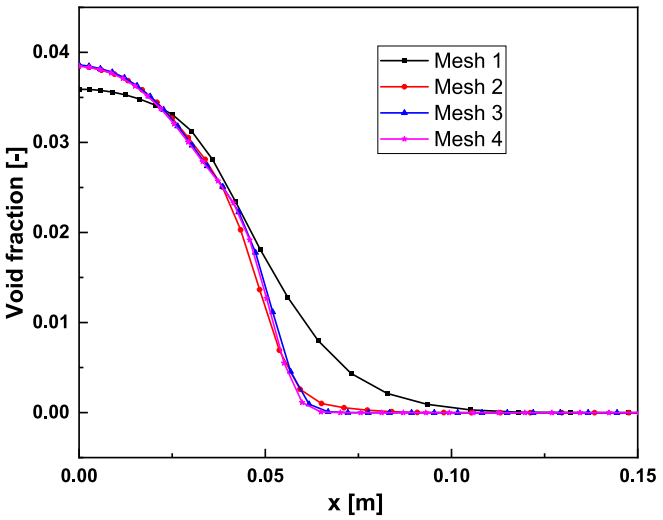

Fig. 3. Mesh sensitivity study.

300 mm. The deviation of the void fraction distribution may be due to the constant diameter model which cannot reproduce the physical distribution for various bubble diameters. In the simulation, the bubble diameter is set to 4 mm. Small bubble tends to move towards the wall and form the double-peak or wall-peak distribution due to the lift force. As for the velocity, the simulation overestimated compared with the experiment above z = 500 mm (Abe et al., 2018). In Fig. 4 (b), although the accuracies at other heights are receptible, the estimation has a large discrepancy at z = 100 mm in such abnormal high inlet velocity.

In experimental study (Abe et al., 2018), after injecting gas from the bottom to form bubbles or jets, they will continue to rise to a higher position, bubble coalescence and break-up occur frequently here, and the bubble diameter varies from less than 1 mm to more than 30 mm. The region below z = 300 mm is observed as the transition from the injection region to the swarm region in this case. Previous work (Paul et al., 1985) shows that the bubble size in the stable bubble swarm region shows a log-normal distribution with most frequent diameter equal to 5.7 mm and does not change significantly even with various gas volume flow rates and bubble rising heights. In this work, the constant bubble diameter is also used for simplification. One of the reasons for the prediction deviation is owing to the constant bubble diameter model which cannot reflect the physical bubble diameter distribution. Because the bubble diameter is a key parameter in the interfacial force models, such as drag force and lift force which are very important to simulate the two-phase flow. The constant bubble diameter model cannot accurately reproduce the morphology change and may distort the force calculation and then affects the simulation results. Utilizing an assumed constant bubble diameter in this research is a simplification and compromise. Therefore, the simulation should be improved further by introducing the bubble size distribution model into the pool scrubbing process using methods such as PBM and IATE. Another reason may be that the interfacial force model and correlations based on the empirical results is not fully suitable for high inlet velocity under pool scrubbing conditions because it depends on the different flow patterns and conditions. The results suggest that the application of the baseline model presents good feasibility to catch the flow characteristics and tendencies. Improved results should be possible by applying the bubble diameter distribution model and improving the empirical force model under the pool scrubbing conditions.

3.2. Evaluation of Lagrangian approach

Since it is difficult to track the individual bubble motion and record the residence time in experiments, the evaluation of Lagrangian

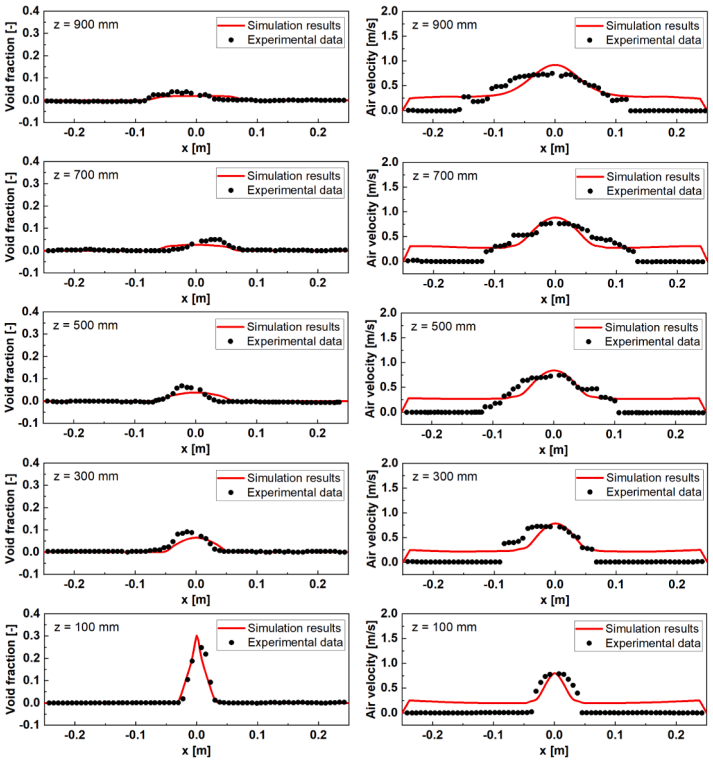

(a) 5 m/s

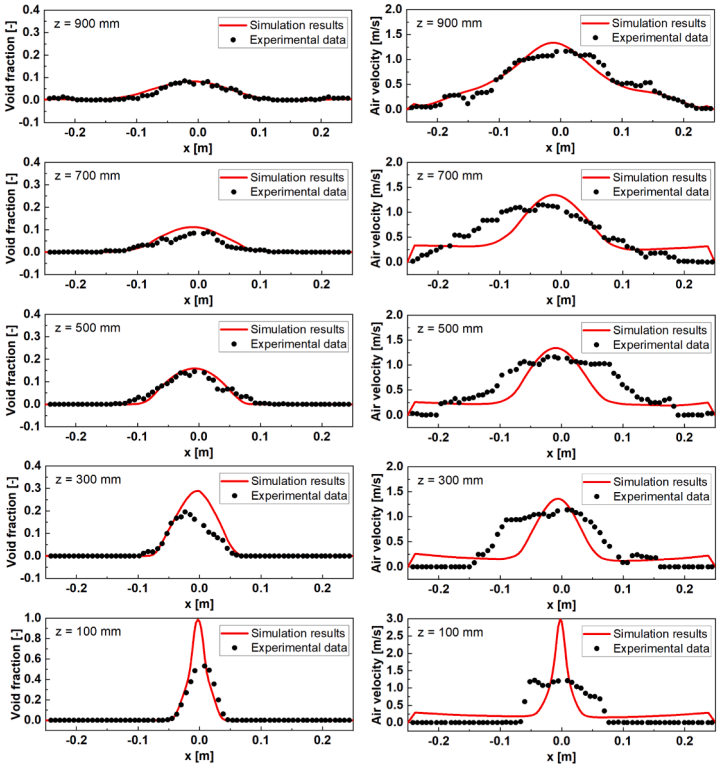

(b) 50 m/s

Fig. 4. Comparison of calculated void fraction and air velocity with experimental data (Abe et al., 2018) for case 1 and 4.

approach will be carried out by comparing with Euler-Euler results. Fig. 5 shows the comparison of vertical velocity at z = 1000 mm in Euler-Euler and Lagrangian approach in case 1. The bubble velocity calculated by Lagrangian approach is almost the same as Euler-Euler results except for the wall region. This is because the air motion in the Lagrangian approach evolves according to the water velocity and has the same tendency as water velocity.

Fig. 6 shows the trajectory of one bubble at x-z plane which was injected at the position of (0.0013, 0.0013, 0.3). The obtained bubble trajectory represents the mean trajectory. Since the water flow field is time-averaged, the velocity fluctuation (shown in Fig. 7) especially in lateral direction cannot be caught, resulting in smaller horizontal displacements. The calculated bubble velocity is larger than the actual position far away from the central axis, and the result of bubble residence time is conservative. And the discrepancy is larger in higher inlet velocity. Nevertheless, due to the accurate prediction of vertical velocity, the residence time of bubbles can be obtained quickly and easily through this method without spending a lot of resources to simulate the real movement of a large number of bubbles and try to get statistically significant results.

4. Application of the Euler-Euler-Lagrangian approach

The above sections show that the Euler-Euler-Lagrangian approach is feasible to catch flow behaviors, bubble motion, and bubble residence time. And then it is applied to various cases with different pool scrubbing conditions, i.e. air inlet velocity, bubble diameter, volume flow rate, and submergence height to investigate swarm bubble behavior as well as the bubble residence time. Table 4 summarizes the simulation cases. Case 1 is the reference case. Case 2–4 are aimed to study the effect of air inlet velocity, Case 5–8 the effect of bubble diameter, Case 9–10 the effect of submergence height, Case 11–12 the effect of volume flow rate at the same velocity.

4.1. Void fraction

Fig. 8 shows the void fraction profiles for the minimum and maximum volume flow rates (case 1 and 4). The flow will form the inverted cone flow structure after the air is injected to the water pool from the bottom and fully develops. With the height increases, the flow spreads to a larger range due to the intensive momentum and energy exchange. The spread edge is positioned by the cell center, and it is determined that the air reaches the spread edge when the local

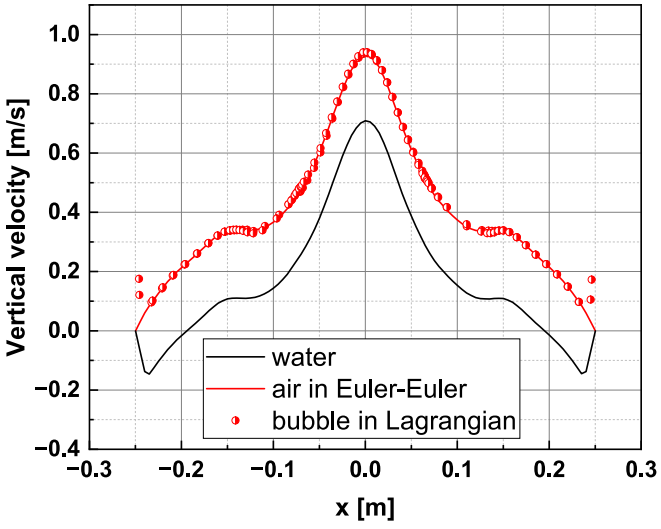

Fig. 5. Comparison of vertical velocity in Euler-Euler and Lagrangian approach at z = 1000 mm.

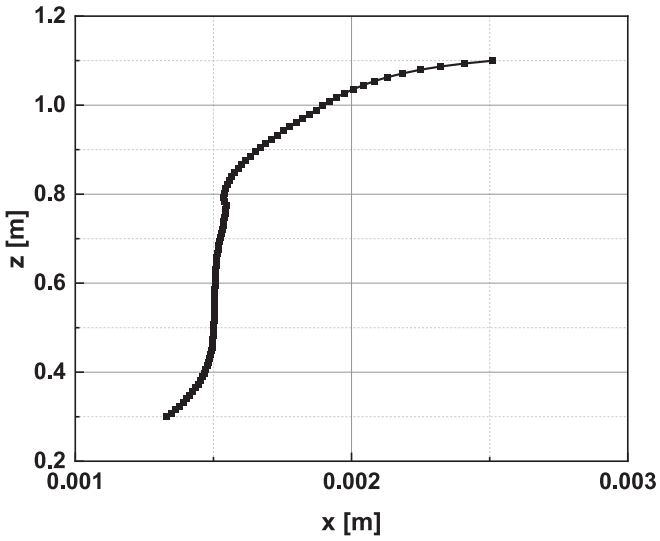

Fig. 6. Bubble trajectory in x-z plane.

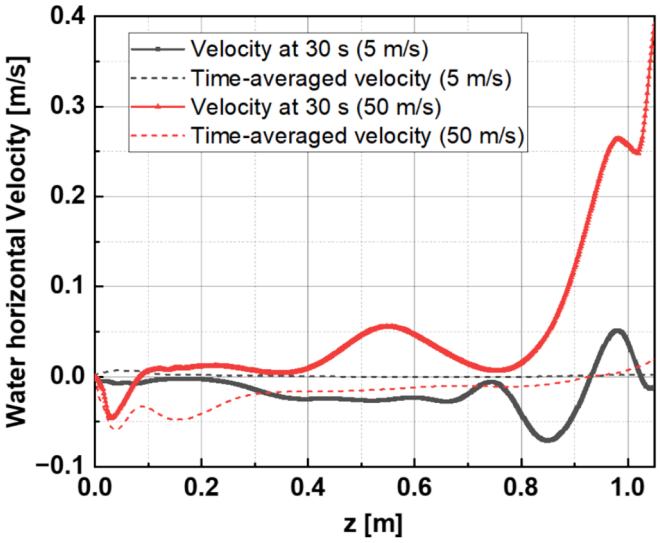

Fig. 7. Comparison of transient and time-averaged water horizontal velocity.

Table 4
Summary of simulation cases.

Case Num.	Air inlet velocity [m/s]	Bubble diameter [mm]	Submergence (h_0) [m]	Volume flow rate [L/min]
1	5	4	1.1	8.48
2	10	4	1.1	16.96
3	25	4	1.1	42.40
4	50	4	1.1	84.80
5	5	3	1.1	8.48
6	5	5	1.1	8.48
7	5	6	1.1	8.48
8	5	8	1.1	8.48
9	5	4	2.1	8.48
10	5	4	3.1	8.48
11	5	4	1.1	16.96
12	10	4	1.1	8.48

equivalent bubble number (before rounding) is equal to 0.4–0.6. The spread radius is obtained by averaging the distances from the cell center positions to the central axis. And with the increase of air inlet velocity

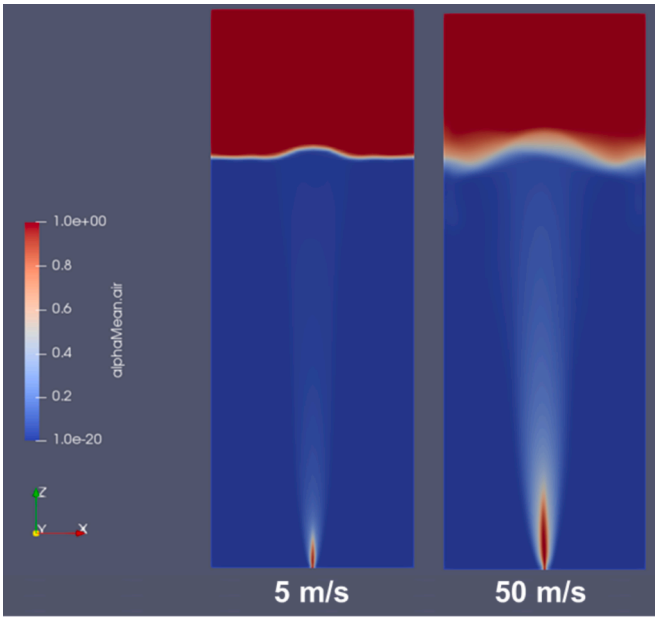

Fig. 8. Time-averaged void fraction profiles for case 1 and 4.

and corresponding volume flow rate, the spread radius also increases as shown in Fig. 9. It is noticed that in case 3 and 4, the air spreads to a larger range near the water surface due to some of small bubbles move downwards with the water recirculation. The mainstream of the inverted cone flow structure could be called as core region. The recirculation region represents the spread range due to recirculation. The recirculation width is about 0.06 m and 0.08 m above z = 900 mm near the wall in case 3 and 4, respectively. The reasons for this phenomenon will be explained later in combination with the results of velocity and flow field. Fig. 10 shows the void fraction distribution for different bubble diameters at z = 500 mm. Due to the effect of lift force, the smaller bubbles tend to move toward the wall, and larger bubbles flow to the center region. With the increase of the bubble diameter, air spreads to a larger range but with a smaller peak value. The void fraction even shows a double-peak distribution when the bubble diameter is 3 mm. The comparisons of void fraction distribution at z = 500 mm and spread radius in the cases of 1, 2, 11 and 12 are shown in Fig. 11 and Fig. 12. It could be seen that in the same volume flow rate, the air inlet velocity has a little effect on flow develop even the air inlet velocity doubles by changing the

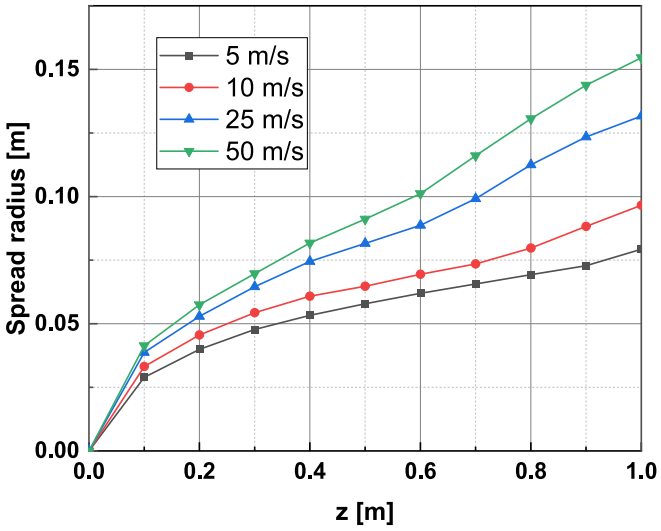

Fig. 9. Spread radius in core region for different air inlet velocities.

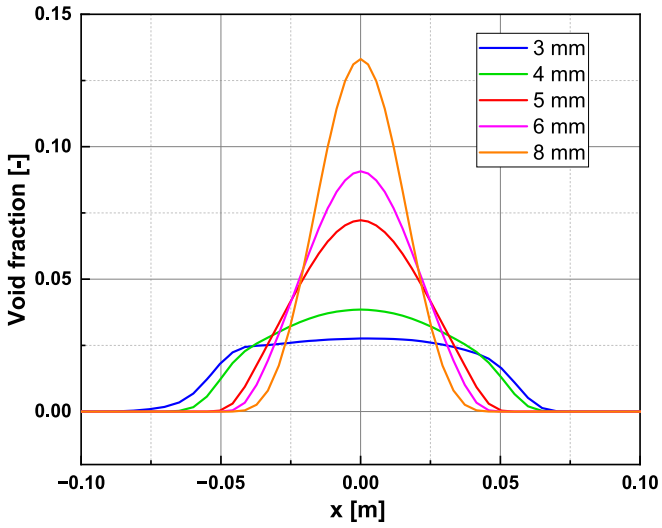

Fig. 10. Void fraction distribution for different bubble diameters (z = 500 mm).

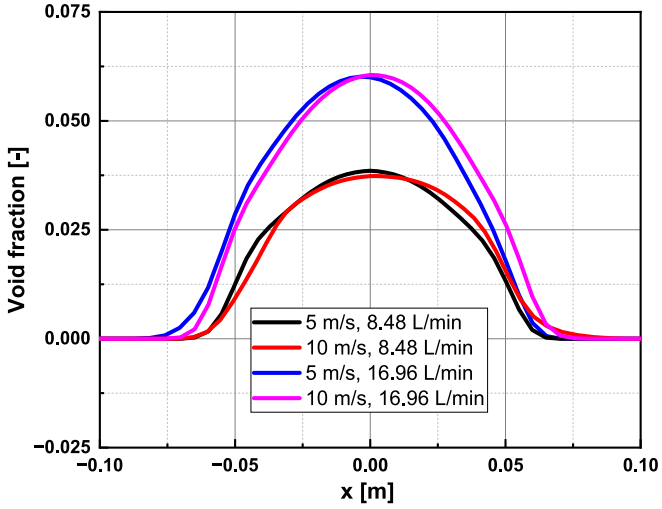

Fig. 11. Void fraction distribution for case 1, 2, 11 and 12 (z = 500 mm).

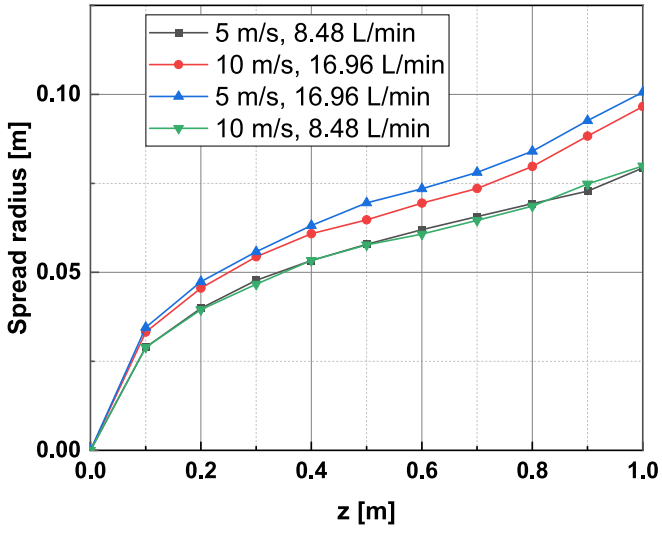

Fig. 12. Spread radius for core region for case 1, 2, 11 and 12.

nozzle size. Under the same flow rate, the air-jet flow development shows a similar distribution. The explanation will be given in section 4.2 combining the velocity field information.

4.2. Velocity field

Fig. 13 and Fig. 14 show the air and water vertical velocity distribution in different heights in case 1. Since the flow is dominated by bubble-induced turbulence, the water velocity is smaller than air at the same position. The slip velocity between air and water is around 0.21 m/s. Compared with the spread radius in Fig. 9, it can be found that the void fraction distribution is narrower than air velocity at the same height. It may be due to the fact that some small bubbles still have a relatively high rising velocity in a short period of time after leaving the core region. Then the velocity drops rapidly under the action of resistance and gravity.

Fig. 15 shows the air velocity distribution for different bubble diameters at z = 500 mm. Smaller bubbles experience less buoyancy, resulting in lower rising velocity in the core region. Combining Fig. 10, it can be seen that since the spread radius of small-diameter bubbles is larger, air velocity is still affected by the velocity field of water caused by the buoyancy of the bubble swarm. Therefore, in the outer region, the velocity of smaller bubbles is greater than the velocity of large-diameter bubbles here which is approximately equal to the terminal velocity of a single bubble in still water.

And Fig. 16 illustrates comparison for case combinations of 1, 2, 11 and 12. The inlet velocity has more effect on velocity distribution than void fraction distribution compared with Fig. 11. However, there is still no obvious difference and the distribution is also similar in the same volume flow rates. Because different inlet velocities will lead to different velocity developments at the beginning. Due to the deceleration effect dominated by drag force, the velocities will soon become similar. At this time, bubbles with the same diameter will receive similar forces under the same flow rate, and then show similar distributions in both void fraction and velocity. This also provides ideas for subsequent research, which can reduce the inlet velocity by increasing the nozzle area and obtain a similar flow field for same volume flow rate to avoid situations where the interfacial force models may not be applicable at high gas inlet velocity. However, since it is assumed as the mono-dispersed flow in the simulation, the effect of air inlet velocity on the flow pattern cannot be observed.

Fig. 17 shows the comparison of time-averaged air velocity vector between case 1, 3 and 4. With the volume flow rate increasing, the

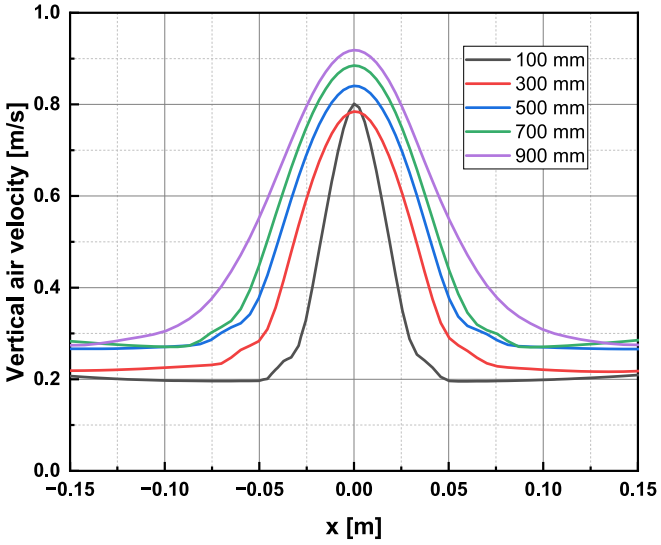

Fig. 13. Vertical air velocity distribution for case 1.

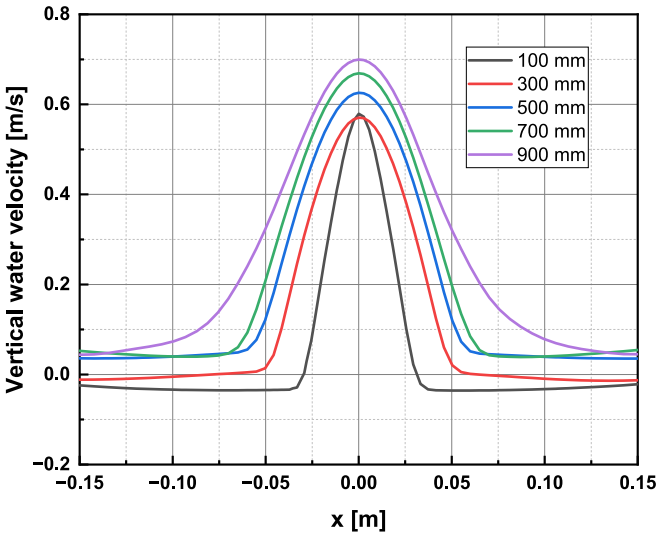

Fig. 14. Vertical water velocity distribution for case 1.

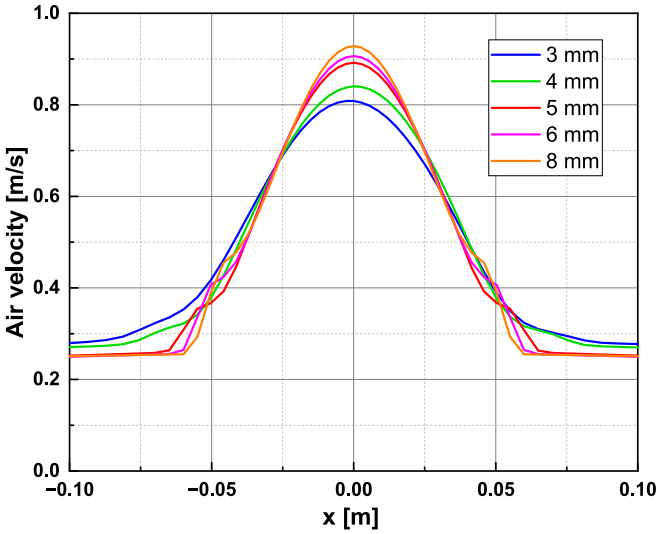

Fig. 15. Air velocity distribution for different bubble diameters (z = 500 mm).

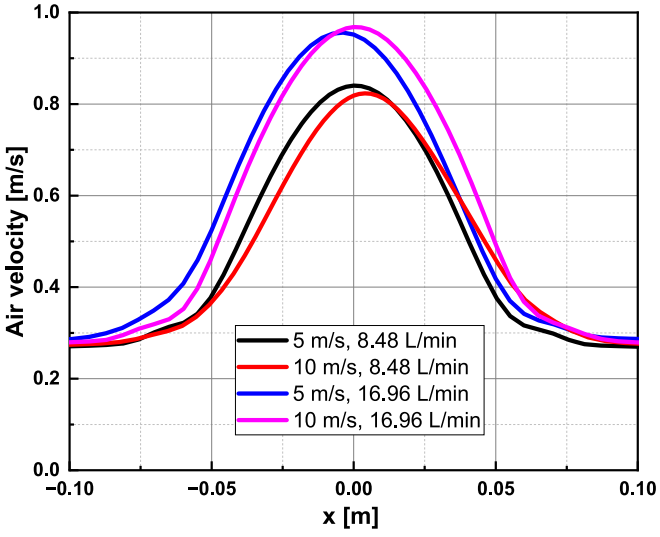

Fig. 16. Air velocity distribution for case 1, 2, 11 and 12 (z = 500 mm).

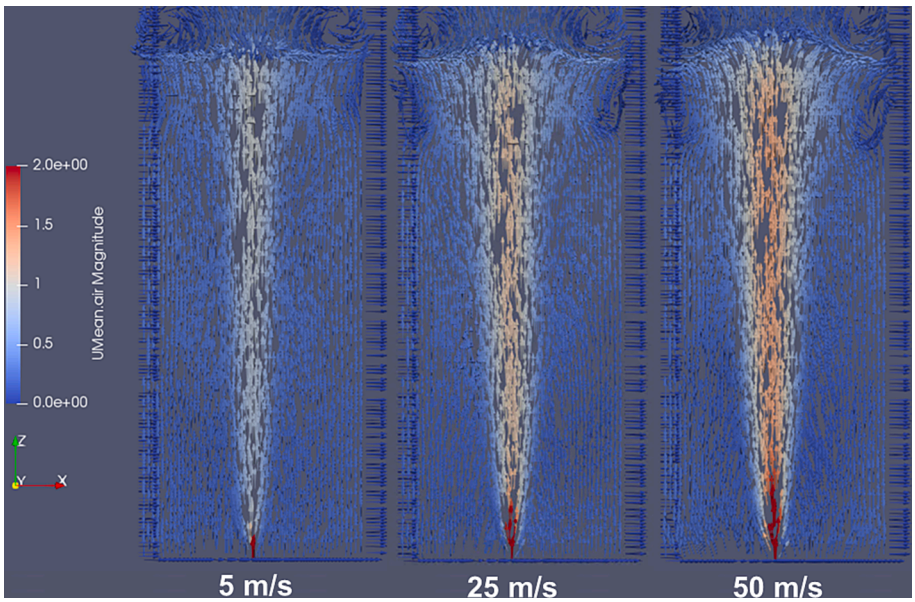

Fig. 17. Time-averaged air velocity vector at x-z plane for case 1, 3 and 4.

swarm flow develops in a larger horizontal region and has an intensive interaction with water around. Then large amounts of small bubbles generate and move downwards near the surface. Therefore, the air recirculation occurs beneath the water surface and the flow spreads further in the radial direction. The air recirculation could be observed in case 3 and 4. The time-averaged vertical air velocity distribution at z = 1000 mm shown in Fig. 18 also illustrates the air recirculation according to the negative values near the wall. The recirculation could prolong the bubble residence time and more quantitative results of residence time can be found in subsequent analysis.

Fig. 19 illustrates the evolution of velocity through the bubble rising in case 1, and 5–8. From the inlet, the velocity of the gas phase decreases dramatically in the injection region. Velocity drops from 5 m/s to lower than 1 m/s only for the elevation of 100 mm. This is due to the high air inlet velocity leading to a high slip velocity and further the high corresponding drag force, which reduces the air velocity very quickly. Correspondingly, the slip velocity will become smaller, and then the buoyancy force becomes the dominant force and the air accelerates

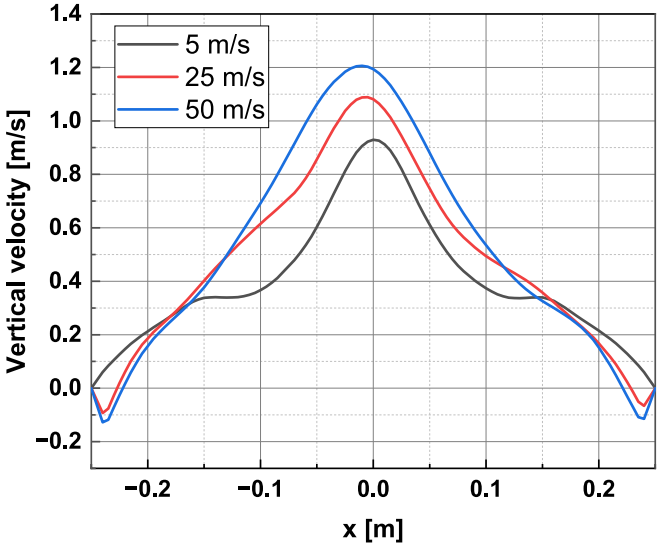

Fig. 18. Comparison of air vertical velocity distribution at z = 1000 mm in different air inlet velocities for case 1, 3 and 4.

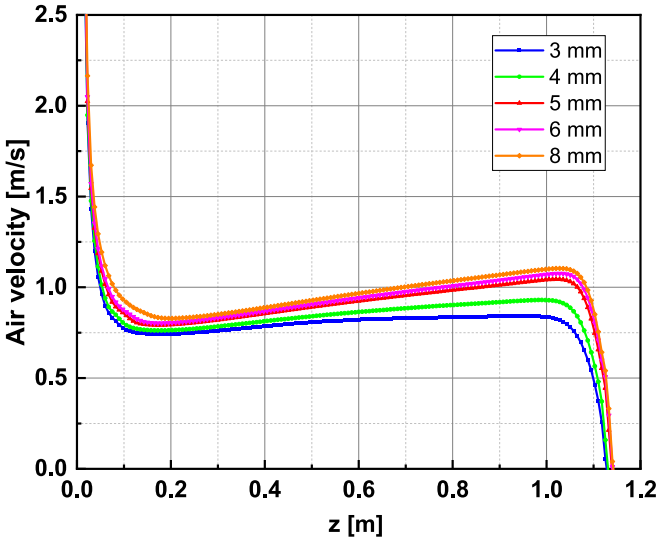

Fig. 19. Time-averaged air velocity at the central axis for case 1, 5–8.

slightly. The larger the bubble diameter, the greater the buoyancy force and the more obvious the acceleration will be. Afterward, as the air continues to rise, the water velocity near the water surface fluctuates greatly, and the value of the drag force and turbulent dispersion force suddenly increase, causing the velocity to decrease rapidly. Above the water surface, buoyancy disappears and deceleration continues to 0. Fig. 20 shows the velocity comparison of different submergence heights. With submergence increases, air spreads to a larger range and accelerates the surrounding water. At the spread edge, the effect is limited and water cannot maintain the velocity due to gravity and will fall quickly. Thus, the water recirculation occurs earlier in the pool not only near the water surface. Also, air forms a double-peak distribution due to lift force. Both of them lead to the decrease of velocity in the central axis.

4.3. Bubble residence time

4.3.1. Radial distribution of bubble residence time

Fig. 21 shows the distribution of residence time with radial injection positions and corresponding bubble injection velocity in case 1 (5 m/s,

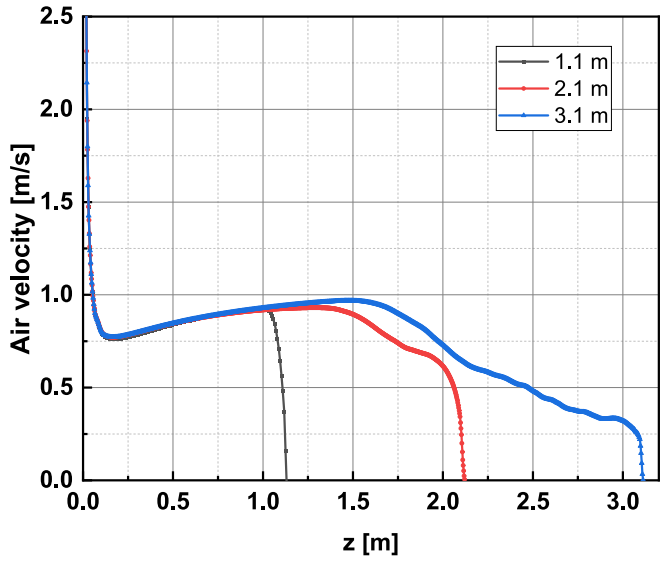

Fig. 20. Time-averaged air velocity at the central axis for case 1, 9 and 10.

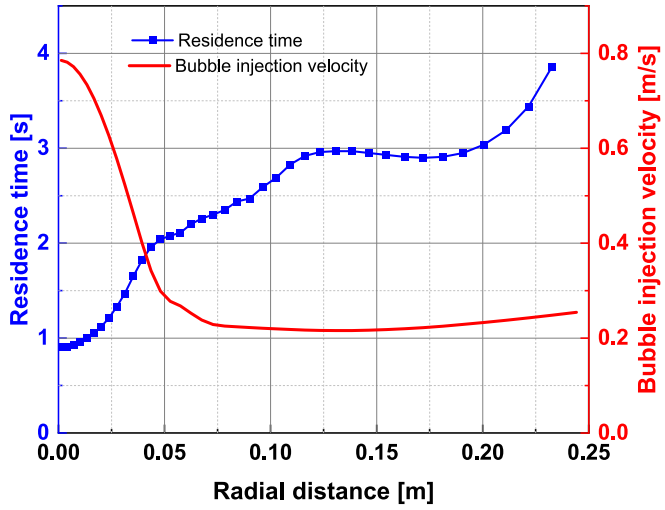

Fig. 21. Residence time versus radial injection position for case 1.

8.48 L/min). It can be seen that the bubble residence time increases as the bubble injection position deviates from the center. The curve could be divided into two parts according to the flow spread region (Fig. 9) and dominant force.

The first part is that bubble injection position in the core region. At the injection height, the spread radius of core region is within 0.05 m for shown case. In this part, the bubble velocity is large and the drag force dominates the bubble motion. Bubbles injected in this radial range stay for a short time in the water pool. There is almost no large difference in residence time for bubbles injected at very central positions (within 0.005 m). For the bubbles injected at the radial position within 0.05 m, residence time increases almost linearly.

The second part is that bubble injected position is not inside the core region. Bubbles from this position have a relatively smaller injection velocity than those of the core region which are mainly driven by buoyancy force and more easily affected by turbulence and secondary flow. In this case, for the radial injection position from 0.05 to 0.1 m, the residence time continues to increase but exponentially. Although these bubbles are not in the core region at the injection height, will firstly take a bit of time to flow along with the water field and travel towards the core region when they rise. Since the core region spreads ranger with height increasing, the bubbles originally outer of the core region gradually merge into it with the bubble rising. The farther away from the center, the longer it takes to reach the core region part. When coming to the bubbles injected at the radial injection position from 0.1 m to 0.2 m, the water velocity is near zero and bubbles travel nearly at the terminal velocity. Therefore, they stay the similar time in the liquid pool. For bubble with radial injection position from 0.2 m to the wall, the residence time has a significant increase with the radial distance increasing again. This is because the bubbles at these locations will rise to the water circulation region, change their direction of movement, and gain more lateral displacement.

Fig. 22 shows the bubble residence time distribution in different air inlet velocities. With the air inlet velocity increasing, there is more intensive and wider circulation in water flow. Especially in the case of 50 m/s, it prolongs the bubble residence time.

4.3.2. Bubble mean residence time

In previous section, the bubble radial distribution for individual bubbles injected at different positions is discussed. This section emphasizes the global bubble mean residence time in the swarm region. In the physical process, the mass flow rate in different positions is different so calculating the mean residence time (*MRT*) weighted by the bubble number is of vital importance. The calculation way of the normalized height and *MRT* could be referred to section 3.1. Fig. 23 shows the comparison of mean, minimum and maximum residence time along with the height increasing. The maximum and minimum values here only consider positions where the equivalent bubble number (N_i) is not equal to 0 which means positions really distribute bubble. The mean value is closer to the minimum *RT* because bubble number, that is, the gas mass flow rate, has a Gaussian distribution in the core region.

The effect of air inlet velocities when keeping volume flow rates the same is shown in Fig. 24. The volume flow rate has a significant effect on mean residence time. An increase in inlet velocity could decrease mean residence time when the nozzle sizes are same while the inlet velocity has limited effect on mean residence time when the flow rate same. The effect of air inlet velocities on the swarm bubble residence time is discussed and shown in Fig. 25. Since bubbles are mainly distributed in the core region, the residence time within the core region has a decisive effect on *MRT** combining with the corresponding bubble residence time distribution in Fig. 22. Worth noting that, the mean residence time values in all four cases are smaller than the predicted results by the model. One reason is mentioned in section 3.2 that using the time-

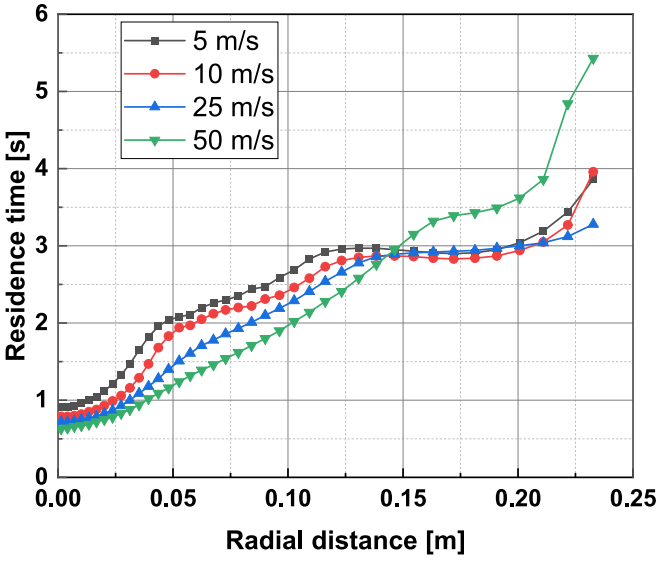

Fig. 22. Residence time versus radial injection position for different inlet air velocities.

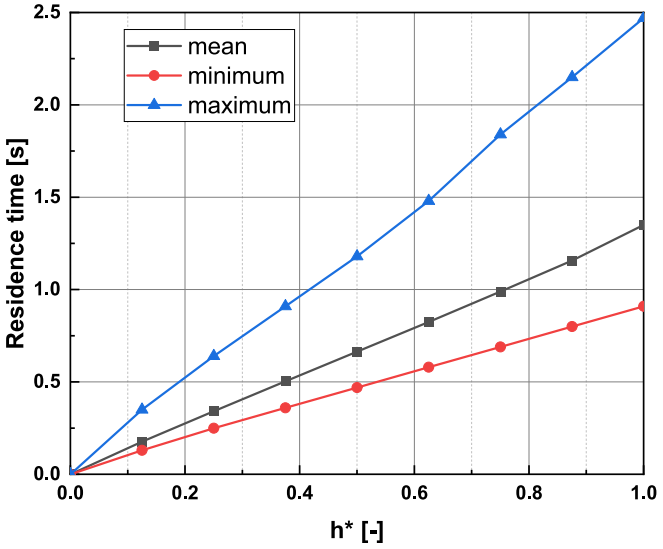

Fig. 23. Comparison of mean, minimum and maximum residence time.

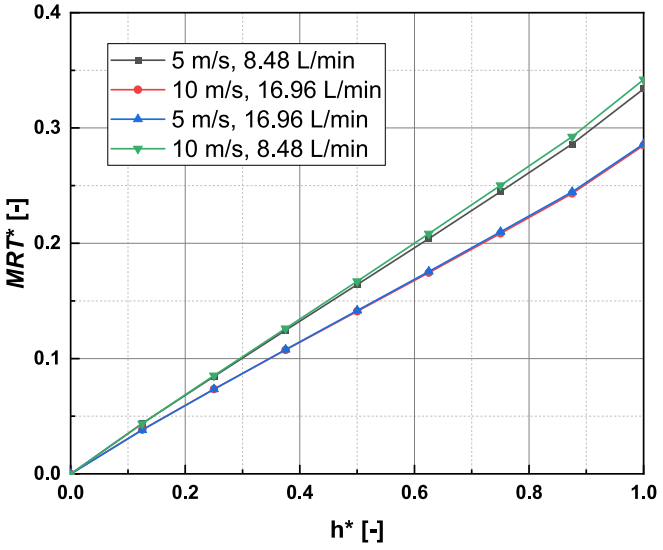

Fig. 24. *MRT** for case 1, 2, 11 and 12.

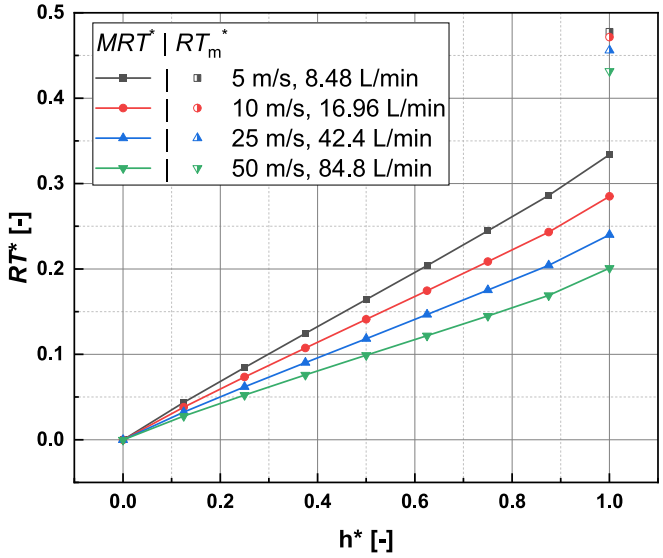

Fig. 25. *RT** for different air inlet velocities.

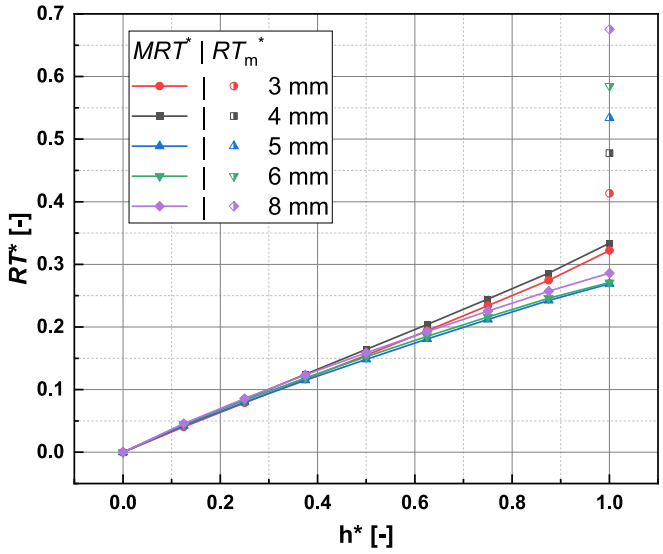

Fig. 26. *RT** for different bubble diameters.

averaged water flow field leads to conservative results. Another is that the model may not be applicable to predict rising velocity at high inlet velocities and volume flow rates because of the flow recirculation according to the comparison with experimental data (Abe et al., 2018).

The effect of bubble diameter on bubble residence time is examined and the results are shown in Fig. 26. According to Fig. 18, smaller bubbles have lower rising velocities and stay longer time in the pool. The big difference in residence time between bubble diameters greater than 5 mm and less than 5 mm was observed. Combining the void fraction and velocity distribution in Figs. 10 and 15, it can be explained that due to the higher average bubble velocity resulting from the higher concentration in core region and higher simulated velocity, the mean residence time of larger bubbles is obviously shorter. In addition, according to Eq. (26), the bubble diameter also affects the dimensionless residence time, so the negative correlation between the simulated physical residence time and the bubble diameter cannot be shown in the figure. For the model results, the differences in the case of different diameters basically come from nondimensionalization, because the effect of bubble diameter on residence time is not considered in the model.

Besides, under the assumption of constant bubble diameter, the bubble break-up and coalescence (especially larger bubble rupture) and bubble size distribution are not considered in this work. There are still large bubbles in the swarm region due to coalescence (Yoshida et al., 2022). Large bubbles with Weber numbers (We_b) greater than 15 are unstable and will break up into smaller bubbles (Paul et al., 1985), in our researched conditions, the critical bubble diameter is about 18.6 mm. According to Fig. 23, the mean residence time is closer to the minimum *RT* because the gas mass flow rate has a Gaussian distribution in the core region, which means the bubbles in the core region have a larger impact on mean residence time. As mentioned before, larger bubbles flow to the center region due to the effect of lift force. Before breaking up, larger bubbles tend to rise faster with a larger velocity than smaller bubbles because it has a larger volume and buoyancy. Therefore, the mean residence time will be smaller when considering large bubbler rupture behavior. If the bubble size distribution is introduced for further improvement, the *MRT* results will be closer to the case of 5 mm. Because *MRT* is calculated and weighted by bubble number (Eq. (22)) and the value would be closer to that in case of the most frequent diameter which is around 5.7 mm (Paul et al., 1985). However, the average velocity will be predicted to be smaller when bubble size

distribution is introduced leading to *MRT* being further smaller and closer to the case of 5 mm.

$$We_b = V_r^2 \frac{\rho_w d_b}{\sigma} \tag{27}$$

where *Vr* is 0.24 m/s for bubble diameter in range of 2–20 mm.

Fig. 27 shows bubble residence time increases with submergence (the rising heights from injection level are 0.8 m, 1.8 m, 2.8 m in submergence of 1.1 m, 2.1 m and 3.1 m). Increasing the submergence height could prolong the bubble residence time significantly. The longer the bubbles stay in the water, the longer they interact with the water, which helps in aerosol decontamination and improves aerosol removal efficiency. *MRT** in higher submergence has an obvious increase after *h** larger than 0.6 leading to the residence time being closer to the model-predicted result. Meanwhile, submergence height has a limited effect on the model-predicted residence time. This is because swarm rising velocity in the model changes slowly with an increase of rising height but simulated residence time increases due to the large velocity drop when the water recirculation occurs shown in Fig. 20.

5. Conclusion

In this work, the Euler-Euler-Lagrangian approach is established to investigate swarm flow behavior and bubble residence time under pool scrubbing conditions. The main conclusions are as follows:

(1) The Euler-Euler-Lagrangian approach is feasible to predict the bubble dynamics and residence time in the liquid pool. The Euler-Euler approach with the baseline model is used for the simulation of two-phase flow field. The results obtained show an acceptable agreement in general tendency with the experimental data, although further improvement should be performed by implementing the bubble diameter distribution model. The methodology of applying the Lagrangian approach based on the obtained flow field to trace bubble trajectory is utilized and could obtain the bubble residence time. Since the velocity fluctuation cannot be caught by time-averaged flow field, the result of bubble residence time is conservative.

(2) The radial distribution of bubble residence time is dependent on the initial position, where bubbles deviating from the central region could remain inside the liquid pool for a larger physical time, up to 5 times longer than at the center position. Mean residence time is closer to the minimum residence time since bubbles are mainly distributed in the center of the region.

(3) The effects of air inlet velocity, bubble diameter, volume flow rate, and submergence height on bubble residence time are fully discussed. With the increase of air velocity, more intensive circulation in water flow could enlarge the bubble residence time in circulation region. Smaller size of bubble leads to longer bubble residence time. The volume flow rate has a significant effect on bubble residence time. When the nozzle sizes are same, an increase of inlet velocity could decrease residence time. However, the inlet velocity has limit effect on residence time when the flow rate same. Increasing the submergence is an effective way to prolong the bubble residence time. And comparison between simulated residence time and predicted results by the existing model shows the discrepancy of simulated residence time and limitations of existing model at high volume flow rate and high submergence.

In general, the present CFD method shows good potential in simulating bubble residence time. Future work will emphasis on modeling the residence time to improve the predict aerosol decontamination factor based on the developing CFD data set.

Declaration of competing interest

The authors declare that they have no known competing financial interests or personal relationships that could have appeared to influence the work reported in this paper.

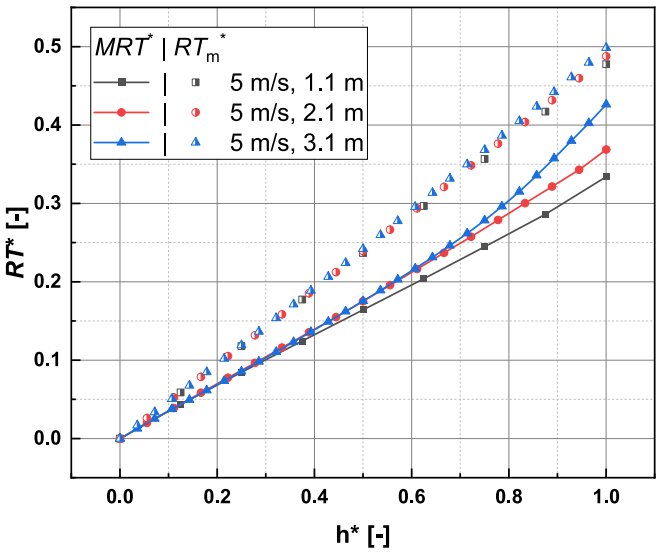

Fig. 27. *RT** for different submergence heights.

Data availability

Data will be made available on request.

Acknowledgements

This work is funded by the German Federal Ministry for the Environment, Nature Conservation, Nuclear Safety and Consumer Protection (BMUV) under grant number 1501652 based on a decision of the German Bundestag. The scholarship from Sino-German (CSC-DAAD) Postdoc Scholarship Program, 2021 (57575640) for the first author is appreciated.

References

Abe, Y., Fujiwara, K., Saito, S., et al., 2018. Bubble dynamics with aerosol during pool scrubbing. Nucl. Eng. Des. 337, 96–107. https://doi.org/10.1016/j.nucengdes.2018.06.017.

Bicer, E., Cho, H.K., Honga, S.J., 2021. CFD simulation of high inlet velocity air flow into a large tank at pool scrubbing conditions. Transactions of the Korean Nuclear Society Virtual Autumn Meeting.

Bicer, E., Hong, S.-J., Jeon, S.-S., 2023. Bubble diameter evaluation in pool scrubbing geometries. Proceedings of ICAPP.

Burns, A.D., Frank, T., Hamill, I., Shi, J.M., 2004. The Favre averaged drag model for turbulent dispersion in Eulerian multi-phase flows. Proceedings of the 5th International Conference on Multiphase Flow 4, 1–17.

Chai, X., Cheng, X., 2015. Wake acceleration effect on spherical bubbles aligned in-line. Prog. Nucl. Energy 80, 74–79. https://doi.org/10.1016/j.pnucene.2014.11.025.

Crowe, C., Schwarzkopf, J., Sommerfeld, M.M., Tsuji, Y., 2011. Multiphase Flows with Droplets and Particles. https://doi.org/10.1201/b11103.

Daivies, R.M., Taylor, G.I., 1950. The mechanics of large bubbles rising through extended liquid in tubes. Proceedings of the Royal Society of London. Series A, Mathematical and Physical Sciences 200, 375–390. https://doi.org/10.1098/rspa.1950.0023.

Gao, S., Fu, Y., Sun, D., Mei, Q., 2017. Comparison research on different aerosol pool scrubbing models. International Conference on Nuclear Engineering, American Society of Mechanical Engineers 57854. https://doi.org/10.1115/ICONE25-66540.V007T10A012.

Hänsch, S., Evdokimov, I., Schlegel, F., Lucas, D., 2021. A workflow for the sustainable development of closure models for bubbly flows. Chem. Eng. Sci. 244. https://doi.org/10.1016/j.ces.2021.116807.

Hessenkemper, H., Ziegenhein, T., Rzehak, R., Lucas, D., Tomiyama, A., 2021. Lift force coefficient of ellipsoidal single bubbles in water. Int. J. Multiph. Flow 138, 103587. https://doi.org/10.1016/j.ijmultiphaseflow.2021.103587.

Hosokawa, S., Tomiyama, A., Misaki, S., Hamada, T., 2002. Lateral migration of single bubbles due to the presence of wall. Proceedings of the ASME Fluids Engineering Division Summer Meeting 36150, 855–860. https://doi.org/10.1115/FEDSM2002-31148.

Ishii, M., Zuber, N., 1979. Drag coefficient and relative velocity in bubbly, droplet or particulate flows. AIChE J 25, 843–855. https://doi.org/10.1002/aic.690250513.

Le Moullec, Y., Potier, O., Gentric, C., Pierre, L.J., 2008. Flow field and residence time distribution simulation of a cross-flow gas–liquid wastewater treatment reactor using

CFD. Chem. Eng. Sci. 63 (9), 2436–2449. https://doi.org/10.1016/j.ces.2008.01.029.

Li, S., Apanasevich, P., Liao, Y., 2023. Euler-Euler CFD simulation of high velocity gas injection at pool scrubbing conditions. Exp. Comput. Multiph. Flow 5, 365–380. https://doi.org/10.1007/s42757-022-0149-3.

Liao, Y., Li, S., 2023. Capture the morphology transfer process in a pool-scrubbing column with a hybrid multi-field two-fluid model. In: 20th International Topical Meeting on Nuclear Reactor Thermal Hydraulics (NURETH-20). https://doi.org/10.13182/NURETH20-40233.

Liao, Y., Li, J., Lucas, D., 2022. Investigation on pool-scrubbing hydrodynamics with VOF interface-capturing method. Nucl. Eng. Des. 390, 111713. https://doi.org/10.1016/j.nucengdes.2022.111713.

Ma, T., Santarelli, C., Ziegenhein, T., Lucas, D., Fröhlich, J., 2017. Direct numerical simulation-based Reynolds-averaged closure for bubble-induced turbulence. Phys. Rev. Fluids 2, 034301. https://doi.org/10.1103/PhysRevFluids.2.034301.

Mei, Z., Kong, F., Cheng, X., 2022. Modeling of submicron particle transport based on VOF-LPT method. Chem. Eng. Sci. 264, 118168. https://doi.org/10.1016/j.ces.2022.118168.

Menter, F., Kuntz, M., Langtry, R., 2003. Ten years of industrial experience with the SST turbulence model. Turbulence, Heat and Mass Transfer 4, 625–632.

Owczarski, P.C., Burk, K.W., 1991. SPARC-90: A code for calculating fission product capture in suppression pools. NUREG/CR-5765 57–65. https://doi.org/10.2172/6120360.

Paul D.D., Flanigan L.D., Cunnane J.C., Cudnik R.A., Collier R.P., Ohlberg R.N., 1985. Radionuclide scrubbing in water pools–gas-liquid hydrodynamics. NP-4113-SR, (ANS Topical Meeting, Snowbird, Utah, 1984), Electric Power Research Institute, Palo Alto, California.

Yan, X., Zhou, Y., Diao, H., et al., 2020. Development of mathematical model for aerosol deposition under jet condition. Ann. Nucl. Energy 142, 107394. https://doi.org/10.1016/j.anucene.2020.107394.

Yoshida, K., Fujiwara, K., Nakamura, Y., Kaneko, A., Abe, Y., 2022. Experimental study of interfacial area of bubble plume based on bubble tracking by wire-mesh sensor. Nucl. Eng. Des. 388. https://doi.org/10.1016/j.nucengdes.2021.111645.